Contents lists available at ScienceDirect

Transactions of Nonferrous Metals Society of China

36(2026) 309−322

www.tnmsc.cn

Hydrothermal conversion from hydrogarnet to hydroandradite based on alumina recovery from red mud

Hong-fei WU [a,b,c], Xiao-lin PAN [a,b,c,*], Ji-long LIU [a,b,c], Feng QIU [a,b,c], Tun HE [b], Hai-yan YU [a,b,c]

[a] Key Laboratory for Ecological Metallurgy of Multimetallic Mineral (Ministry of Education), Northeastern University, Shenyang 110819, China;

[b] School of Metallurgy, Northeastern University, Shenyang 110819, China;

[c] Key Laboratory for Recycling of Nonferrous Metal Resources (Shenyang), Shenyang 110819, China

Abstract: To synergistically recover alumina and alkali from red mud (RM), the structural stability and conversion mechanism of hydroandradite (HA) from hydrogarnet (HG) were investigated via the First-principles, XRF, XRD, PSD and SEM methods, and a novel hydrothermal process based on the conversion principle was finally proposed. The crystal structure simulation shows that the HA with varied silicon saturation coefficients is more stable than HG, and the HA with a high iron substitution coefficient is more difficult to be converted from HG. The (110) plane of Fe_2O_3 is easier to combine with HG to form HA, and the binding energy is 81.93 kJ/mol. The effects of raw material ratio, solution concentration and hydrothermal parameters on the conversion from HG to HA were revealed, and the optimal conditions for the alumina recovery were obtained. The recovery efficiencies of alumina and Na_2O from the RM are 63.06% and 97.34%, respectively, and the Na_2O content in the treated RM is only 0.13%.

Keywords: hydrogarnet; hydroandradite; structural stability; hydrothermal conversion; red mud

1 Introduction

Nearly 60% of the global alumina in 2023 was produced in China, and the storage of red mud (RM) generated from the alumina industry has reached over 1.5 billion tons with an annual growth rate of over 100 million tons [1,2]. As most of the bauxite in China belongs to middle- or low-grade diasporic bauxite, the annual discharge amount of diasporic-bauxite-type RM is above 50 million tons [3,4]. To improve the overall production quality and alumina extraction efficiency, it is necessary to add lime during the Bayer digestion process [5,6], which can reduce the alkali consumption and lead to the formation of a desilication product (DSP) named hydrogarnet (HG, $3CaO{\cdot}Al_2O_3{\cdot}xSiO_2{\cdot}(6-2x)H_2O$, $0<x\leq3$) in RM [7,8]. The chemical reactions responsible for the HG formation during the desilication process are illustrated in Eqs. (1) and (2) [9,10]. The HG crystal belongs to the space group of *Ia3d* with a cubic structure, in which the positions of Ca^{2+} and Al^{3+} ions are symmetrically fixed, and the tetrahedral skeleton of $[SiO_4]^{4-}$ ions are partially or completely replaced by OH^- ions [11]. Moreover, as the main DSP in $Na_2O-Al_2O_3-SiO_2-H_2O$ system, the sodium aluminosilicate hydrate dissolved in sodium aluminate solution releases $Al(OH)_4^-$ and $SiO_2(OH)_2^{2-}$ ions, and then the latter reacts with the preformed tri-calcium aluminate hydrate ($3CaO{\cdot}Al_2O_3{\cdot}6H_2O$) from $Al(OH)_4^-$ ion and $Ca(OH)_2$ to form HG [6,9]:

Corresponding author: *Xiao-lin PAN, Tel: +86-24-83686460, E-mail: panxl@smm.neu.edu.cn

https://doi.org/10.1016/S1003-6326(25)66966-4

Received 3 June 2024; accepted 21 January 2025

1003-6326/© 2026 The Nonferrous Metals Society of China. Published by Elsevier Ltd & Science Press

This is an open access article under the CC BY-NC-ND license (http://creativecommons.org/licenses/by-nc-nd/4.0/)

$$NaAl(OH)_4+Ca(OH)_2\rightarrow 3CaO\cdot Al_2O_3\cdot 6H_2O+NaOH \quad (1)$$

$$3CaO\cdot Al_2O_3\cdot 6H_2O+Na_2SiO_3\rightarrow 3CaO\cdot Al_2O_3\cdot xSiO_2\cdot(6-2x)H_2O+NaOH \quad (2)$$

Hydroandradite (HA, $3CaO\cdot Fe_2O_3\cdot nSiO_2\cdot(6-2n)H_2O$, $0<n\leq 3$), as an efficient DSP without Al_2O_3 and Na_2O in theory, represents an ideal target DSP for processing low-grade bauxites and Bayer RM [12,13]. It is formed both by the spontaneous nucleation in sodium aluminate solution and the isomorphic substitution reaction from HG in the presence of $Fe(OH)_4^-$ as given in Eqs. (3) and (4) [14]. The HA crystal with a cubic structure also belongs to the space group of *Ia*3*d*, which is consistent with the HG crystal. In HA, the [SiO_4] tetrahedron is formed by the Si^{4+} ion coordinated with four adjacent O atoms, while the [FeO_6] octahedron is formed by the Fe^{3+} ion coordinated with six adjacent O atoms, both of which are composed of the skeleton of HA [15]. However, the ionic radius of the Fe^{3+} ion is smaller than that of the Al^{3+} ion, and both the Al^{3+} and Fe^{3+} ions are completely isomorphic. So, the HA usually has a chemical formula of $Ca_3(Al_m,Fe_{1-m})_2(SiO_4)_n(OH)_{4(3-n)}$ ($0\leq m\leq 1$, $0<n<3$) through the isomorphic substitution of Al_2O_3 by Fe_2O_3 [16]:

$$NaFe(OH)_4+Ca(OH)_2+Na_2SiO_3+aq\rightarrow 3CaO\cdot Fe_2O_3\cdot xSiO_2\cdot(6-2x)H_2O\downarrow+NaOH \quad (3)$$

$$3CaO\cdot Al_2O_3\cdot xSiO_2\cdot(6-2x)H_2O+NaFe(OH)_4+aq\rightarrow 3CaO\cdot Fe_2O_3\cdot xSiO_2\cdot(6-2x)H_2O\downarrow+NaAl(OH)_4 \quad (4)$$

To realize the conversion of HG to HA, LI et al [12] suggested a hydrothermal method to form HA in RM at 250 °C for 1 h by adding calcium ferrite ($2CaO\cdot Fe_2O_3$), and the main silica-bearing mineral of RM is HA. ZHANG et al [17] employed the iron-poor and iron-rich RM to create HA using the alkali solution with the caustic alkali concentration of 283−362 g/L at 280 °C, and the results show that the content of HA in the leached residue from the iron-rich RM is much higher than that from the iron-poor RM. However, the above-mentioned studies require the iron source additives, such as sodium ferrite or calcium ferrite, which need to be synthesized at high temperatures, resulting in a significant increase in costs. Meanwhile, the high caustic alkali concentration in the alkaline solution used in the hydrothermal conversion process leads to severe corrosion of the equipment and increases the burden on the subsequent evaporation process.

In this work, the alumina was recovered from the synthetic HG targeting the efficient DSP of HA as the final equilibrium phase, and the corresponding structural stability and phase conversion mechanism were systematically investigated. Moreover, the diasporic-bauxite-type RM was treated without iron source additives to recover alumina as well as alkali synchronously under the recommended conditions. A novel hydrothermal process was proposed finally to comprehensively utilize RM, which can provide a technically and economically feasible approach to reduce or even eliminate the adverse effects of RM on the surrounding ecological environment.

2 Experimental

2.1 Raw materials

Sodium silicate ($Na_2SiO_3\cdot 5H_2O$, 99.00%), sodium carbonate (Na_2CO_3, 99.00%), sodium hydroxide (NaOH, 96%), aluminum hydroxide ($Al(OH)_3$, 99.00%), calcium oxide (CaO, 99.00%) and ferric oxide (Fe_2O_3, 99.00%) were used from Aladdin Chemistry Co., Ltd. (Shanghai, China). The diasporic-bauxite-type RM was produced by the Bayer process from Guangxi, China.

2.2 Preparation of samples

HG was prepared by adding CaO into the mixed solution of sodium aluminate and sodium silicate. The sodium silicate solution was prepared by $Na_2SiO_3\cdot 5H_2O$, and the sodium aluminate solution was prepared by dissolving $Al(OH)_3$ in NaOH solution. The concentrations of caustic alkali (in form of Na_2O) and silica in the synthetic sodium aluminate solution were 212.0 and 10.0 g/L, respectively; the caustic ratio (the molar ratio of Na_2O to Al_2O_3, α_K) and the calcium to silicon ratio (the molar ratio of CaO to SiO_2) were 2.0 and 3.0, respectively; the reaction temperatures ranged from 145 to 250 °C and reaction time was 2 h. As most of the diffraction peaks of HG and HA are similar, there are some minor differences between the two phases in the XRD patterns, as shown in Fig. 1(a). The sodium ferrite for the conversion from HG to HA was prepared by roasting Fe_2O_3 and Na_2CO_3 with the same molar ratio at 950 °C for 2 h [13]. The XRD pattern of the synthetic sodium ferrite is illustrated in Fig. 1(b), which is consistent with the standard peaks (ICDD 01-074-1351).

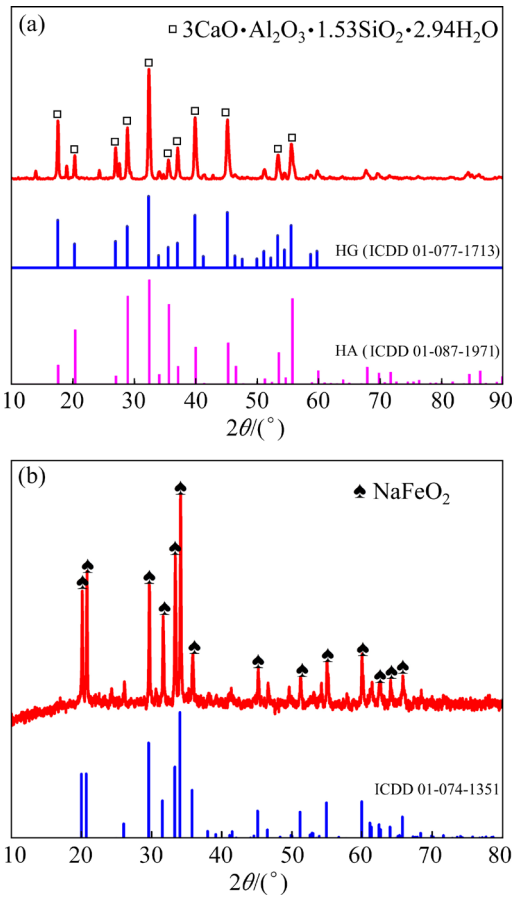

Fig. 1 XRD patterns of HG (a) and sodium ferrite (b)

2.3 Experimental procedure

The CASTEP and MORPHOLOGY modules of Materials Studio software (Accelries Corporation, USA) were used to examine the density of states (DOS), the charge density difference, the surface energy and the binding energy under the generalized gradient approximation (GGA) function [18]. The fine Monkhorst-Pack grid of k points was used to define the accuracy of Brillouin zone sampling. The hydrothermal conversion behavior of diasporic-bauxite-type RM was simulated using synthetic HG, and the RM was then utilized to demonstrate the effectiveness of this technique in practical applications. The hydrothermal reaction was conducted in a 150 mL bomb reactor in the molten-salt autoclave, and the corresponding rotational speed was 45 r/min. The samples after reaction were filtered, washed with distilled water, and dried for 24 h at 100 °C. The iron to alumina ratios referring to the sodium ferrite addition (the molar ratio of Fe_2O_3 in sodium ferrite to that of Al_2O_3 in sodium aluminate solution, F/A) ranged from 0.5 to 1.50; the α_K in sodium aluminate solution was varied from 10 to 30; the reaction temperatures (T) and time (t) ranged 220−300 °C and 5−120 min, respectively. Based on the previous study [6], the contents of various phases in the reaction products could be calculated by the RIR method and chemical compositions. Firstly, the contents of hematite were calculated according to the RIR method, but the HG and HA cannot be analyzed due to their similar intensity of diffraction peaks. Then, the content of HA was calculated from the Fe_2O_3 composition excluding hematite according to its chemical formula. Finally, the content of HG was calculated according to the total contents of CaO, Al_2O_3 and SiO_2 excluding HA based on the chemical formula. The Al_2O_3 recovery efficiency ($\eta_{Al_2O_3}$) from HG or RM was calculated according to Eq. (5):

$$\eta_{A_2O_3}=\frac{(A/S)_0-(A/S)_1}{(A/S)_0}\times 100\% \quad (5)$$

where $(A/S)_0$ and $(A/S)_1$ represent the mass ratio of Al_2O_3 to SiO_2 in HG or RM and reaction product, respectively.

2.4 Characterization of samples

The chemical compositions of the samples were analyzed using an X-ray fluorescence spectrometer (XRF, Philips PW 2404). The phase compositions of samples before and after hydrothermal reactions were determined by an X-ray powder diffractometer (XRD, Philips X'Pert PW3040-60) at 40 kV and 40 mA with a Cu K_α radiation ranging from 10° to 80°. The microstructure was examined using a scanning electron microscopy coupled with an energy dispersive spectrometer (SEM−EDS) on a Zeiss Ultra Plus instrument. The concentrations of silica, alumina and caustic alkali in sodium aluminate solution were determined by the molybdenum blue photometry, EDTA titration and acid-base neutralization titration, respectively. The particle size distribution of the samples was measured by a laser particle size analyzer (PSD, Malvern Hydro 3000) using deionized water as the dispersion medium.

3 Results and discussion

3.1 Structural stability of HG and HA

To reveal the conversion from HG to HA, the First-principles were employed to investigate the structural stability and electronic properties of HG

and HA with varied silicon saturation coefficients. Table 1 presents the formation enthalpy, cell volume and lattice parameters of HG. As the silicon saturation coefficient increases, the lattice parameters increase, while the formation enthalpy gradually decreases. This suggests that the HG with a larger silicon saturation coefficient is more difficult to form. The DOS and charge density difference of HG with varied silicon saturation coefficients are illustrated in Fig. 2. The DOS profiles of HG (Figs. 2(a, c, e, g)) are contributed by the Ca 3d, Ca 4s, Al 3p, Si 3p, O 2s and O 2p state. The directional Si—O, Al—O and Ca—O bonds are formed through the localized hybridization of Si−O, Al−O and Ca−O atoms, as illustrated in Figs. 2(b, d, f, h). The calculated results demonstrate that the Al, Ca, and Si atoms can combine with O atom, and their binding ability increases in the order of Ca, Al and Si. The bond length of HG decreases in the order of Ca—O, Al—O and Si—O, indicating that the Si—O bond is the most stable chemical bond, which is consistent with the previous results [19,20]. It is worth noting that the length of the Ca—O bond in HG increases with the decrease of silicon saturation coefficient, which reveals that the Ca—O bond is most prone to fracture. The above results indicate that the structural stability of HG is significantly affected by the presence of Si—O and Ca—O bonds.

As shown in Fig. 3, the DOS profiles of HA (Figs. 3(a, c)) are contributed by the Ca 3d, Ca 4s, Fe 3d, Si 3p, O 2s and O 2p state. The atomic bonding configuration in HA is similar to that in HG. The directional Si—O bond and Fe—O bond are formed through the localized hybridization of Si−O and Fe−O atoms. The length of the Fe—O bond

Table 1 Calculated results of crystal structure of HG with varied silicon saturation coefficients

HG	Lattice parameter, (a=b=c)/nm	Cell volume/nm^3	Formation enthalpy/eV
$3CaO·Al_2O_3·2.5SiO_2·H_2O$	1.188	1.677	−26296
$3CaO·Al_2O_3·2.16SiO_2·1.68H_2O$	1.194	1.702	−26382
$3CaO·Al_2O_3·2SiO_2·2H_2O$	1.194	1.702	−26398
$3CaO·Al_2O_3·1.53SiO_2·2.94H_2O$	1.217	1.802	−26445

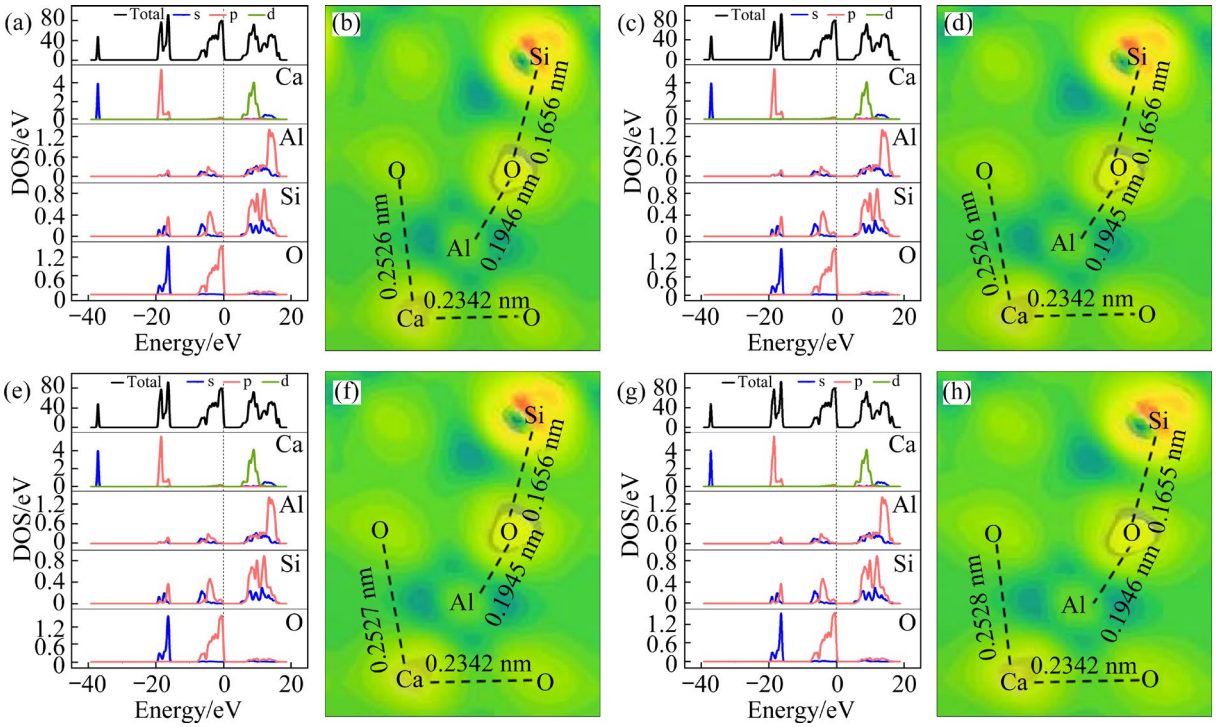

Fig. 2 DOS profiles (a, c, e, g) and bond formation (b, d, f, h) of HG with varied silicon saturation coefficients: (a, b) $3CaO·Al_2O_3·2.5SiO_2·H_2O$; (c, d) $3CaO·Al_2O_3·2.16SiO_2·1.68H_2O$; (e, f) $3CaO·Al_2O_3·2SiO_2·2H_2O$; (g, h) $3CaO·Al_2O_3·1.53SiO_2·2.94H_2O$

(Figs. 3(b, d)) is 0.1971 nm, which is larger than that of Si—O bond (0.1654 and 0.1653 nm). This indicates that the Si—O bond is the most stable chemical bond in HA, which is consistent with the calculated results of HG. Meanwhile, the length of Si—O bond in the HA crystal decreases with the decrease of silicon saturation coefficient. The Si—O bond length in HA with varying coefficients is smaller, suggesting that it has higher stability compared to HG.

The chemical compositions of HG prepared at different temperatures are illustrated in Table 2, and the corresponding formulas were also calculated. The silicon saturation coefficient of HG increases with increasing the reaction temperature. The XRD patterns, particle size distribution (PSD) and morphology of HG are shown in Fig. 4. As observed from Fig. 4(a), the chemical formula of HG is $3CaO{\cdot}Al_2O_3{\cdot}1.53SiO_2{\cdot}2.94H_2O$ when the reaction temperature rises to 250 °C, which is quite different from that formed at 145 °C ($3CaO{\cdot}Al_2O_3{\cdot}0.64SiO_2{\cdot}4.72H_2O$) and 195 °C ($3CaO{\cdot}Al_2O_3{\cdot}SiO_2{\cdot}4H_2O$). The characteristic peaks of HG exhibit a rightward shift as the reaction temperature increases, indicating that the silicon saturation coefficient of HG gradually increases.

When the reaction temperature rises, the specific surface area (SSA) of HG increases, and the particle size range becomes narrower (Fig. 4(b)). The PSD undergoes a conversion from unimodal to trimodal distribution, indicating that the particle size of HG decreases significantly. The HG formed at 195 °C primary agglomerates as staggered sheet particles of ten to hundreds of nanometers, and most crystals grow incompletely due to the low crystallization temperature (Fig. 4(c)). More extensive growth and noticeable agglomeration are observed in HG formed at 250 °C, because of the enhanced crystallinity by increasing the temperature (Fig. 4(d)). These findings indicate that the HG formed at 250 °C has good stability and structural integrity. As the usual digestion temperature for diasporic bauxite is 250−260 °C, the HG produced at 250 °C was used to investigate the reaction and conversion mechanism from HG to HA.

3.2 Conversion behavior from HG to HA

The hydrothermal conversion from synthetic HG to HA in the alkaline solution under various reaction conditions based on the Fe_2O_3–Na_2O–Al_2O_3–CaO–SiO_2–H_2O system was studied, and the synthesized sodium ferrite was added as the iron source during the conversion. The XRD patterns and compositions of the reaction products are presented in Fig. 5. As seen from Fig. 5(a), the main phases are HG ($3CaO{\cdot}Al_2O_3{\cdot}1.53SiO_2{\cdot}2.94H_2O$), HA

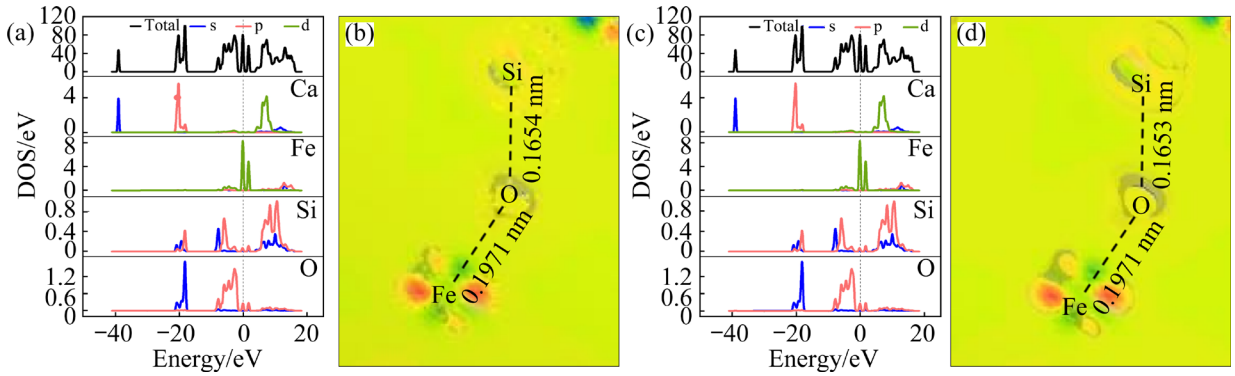

Fig. 3 DOS profiles (a, c) and bond formation (b, d) of HA with varied silicon saturation coefficients: (a, b) $3CaO{\cdot}Fe_2O_3{\cdot}2.5SiO_2{\cdot}H_2O$; (c, d) $3CaO{\cdot}Fe_2O_3{\cdot}1.15SiO_2{\cdot}3.7H_2O$ [15]

Table 2 Chemical compositions of HG prepared at different temperatures

Temperature/°C	Chemical formula	Chemical composition/wt.%			
		CaO	SiO_2	Al_2O_3	H_2O
145	$3CaO{\cdot}Al_2O_3{\cdot}0.64SiO_2{\cdot}4.72H_2O$	41.86	9.13	26.47	22.54
195	$3CaO{\cdot}Al_2O_3{\cdot}SiO_2{\cdot}4H_2O$	41.32	14.66	25.44	18.58
250	$3CaO{\cdot}Al_2O_3{\cdot}1.53SiO_2{\cdot}2.94H_2O$	40.86	24.64	24.61	12.67

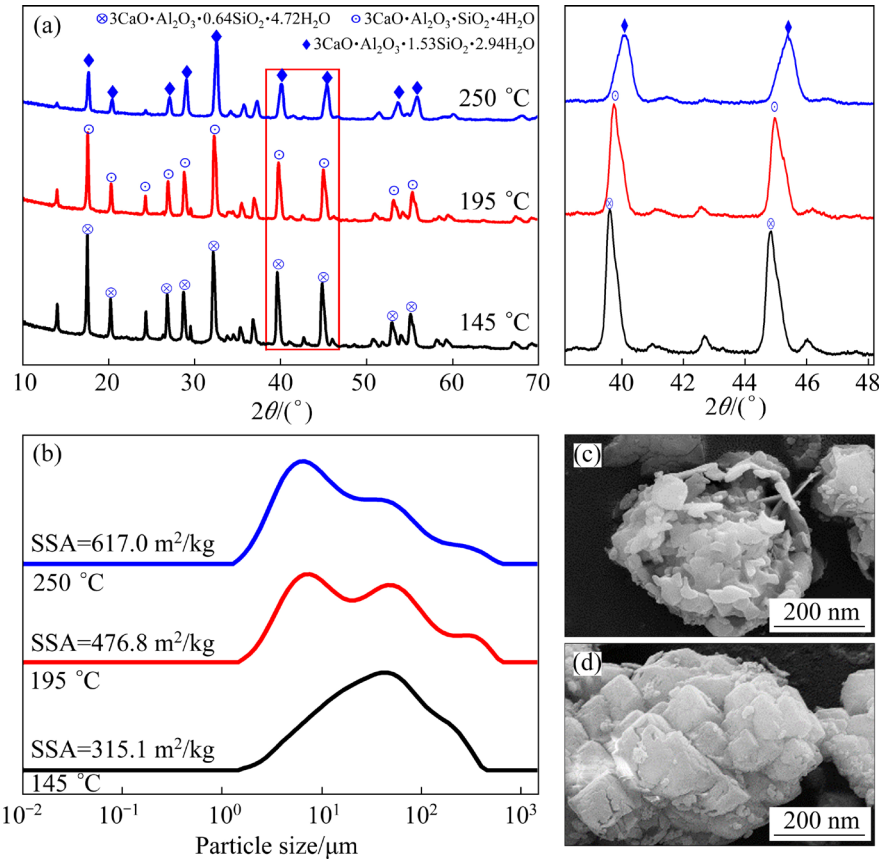

Fig. 4 XRD patterns (a), particle size distribution (b) and morphology of HG prepared at 195 °C (c) and 250 °C (d)

($3CaO{\cdot}0.13Al_2O_3{\cdot}0.87Fe_2O_3{\cdot}1.65SiO_2{\cdot}2.7H_2O$) and hematite ($Fe_2O_3$). The peak intensity of HG decreases with the increasing F/A ratio, while the peak intensity of HA increases. The diffraction peaks of HG are still present as the F/A ratio is 1.25, indicating that the $Al(OH)_4^-$ ion in HG cannot be completely replaced by $Fe(OH)_4^-$ ion in sodium aluminate solution. Figure 5(b) illustrates a significant decrease in the HG content until the F/A ratio reaches 1.0. Conversely, the content of HA initially increases and subsequently stabilizes. Figure 5(c) describes that increasing the reaction temperature promotes the conversion from HG to HA. The new phases of calcium carbonate and calcium hydroxide are formed in the process when the reaction temperature is 300 °C, because of the dissolved Ca^{2+} ions from HG in sodium aluminate solution [21,22]. As seen from Fig. 5(d), the content of HG decreases gradually with rising the reaction temperature, while the content of HA increases gradually, which achieves a maximum of 36.91% when the reaction temperature is 300 °C. The increase in reaction temperature leads to a decrease in the solution viscosity and an increase in the ion diffusion rate [23,24], which enhances the phase conversion from HG to HA.

As presented in Fig. 5(e), the phase conversion exhibits a high speed at 280 °C, resulting in the formation of HA in less than 5 min. Moreover, prolonging the reaction duration from 30 to 60 min significantly enhances the formation of HA. Theoretically, prolonging the reaction time is beneficial for the spontaneous nucleation of HA and the phase conversion from HG to HA. Figure 5(f) illustrates that the HG content initially decreases rapidly and gradually slows down at the late stage. As the reaction time prolongs to 60 min, the phase conversion from HG to HA reaches equilibrium. As presented in Figs. 5(g, h), the contents of HG and HA decrease and increase with the increase of α_K respectively. The increase in α_K, leads to an increase in the equilibrium solubility of alumina in sodium aluminate solution, which enables more alumina to be dissolved [25]. Additionally, the pure NaOH solution with a higher OH^- concentration cannot increase the content of HA.

Figure 6 depicts the Al_2O_3 recovery efficiency during the hydrothermal conversion from HG to HA

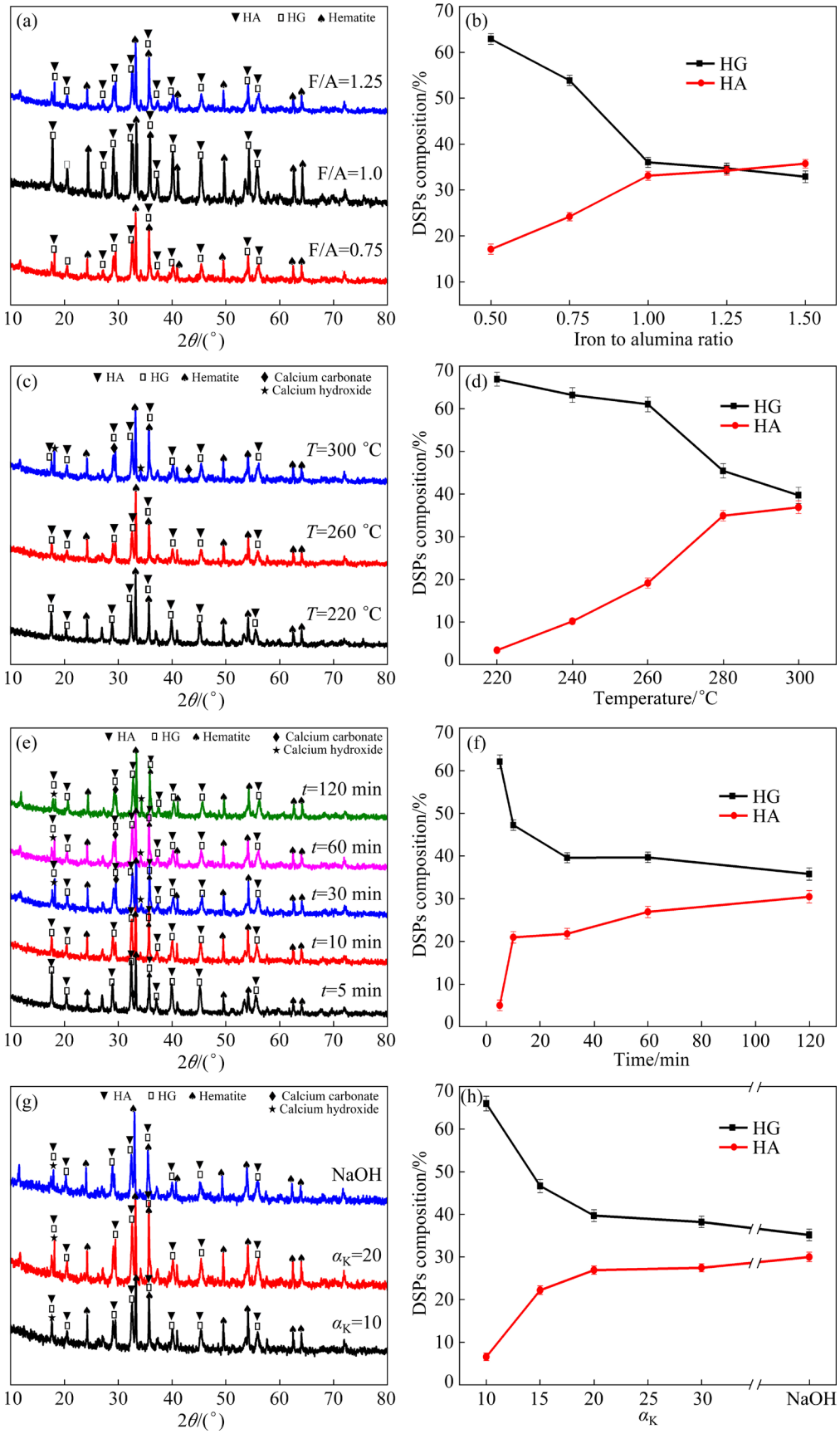

Fig. 5 XRD patterns (a, c, e, g) and compositions (b, d, f, h) of reaction products during conversion from HG to HA: (a, b) Iron to alumina ratio (T=280 °C, t=60 min and α_K=20); (c, d) Reaction temperature (F/A=1, t=60 min and α_K=20); (e, f) Reaction time (F/A=1, T=280 °C and α_K=20); (g, h) α_K (F/A=1, T=280 °C and t=60 min)

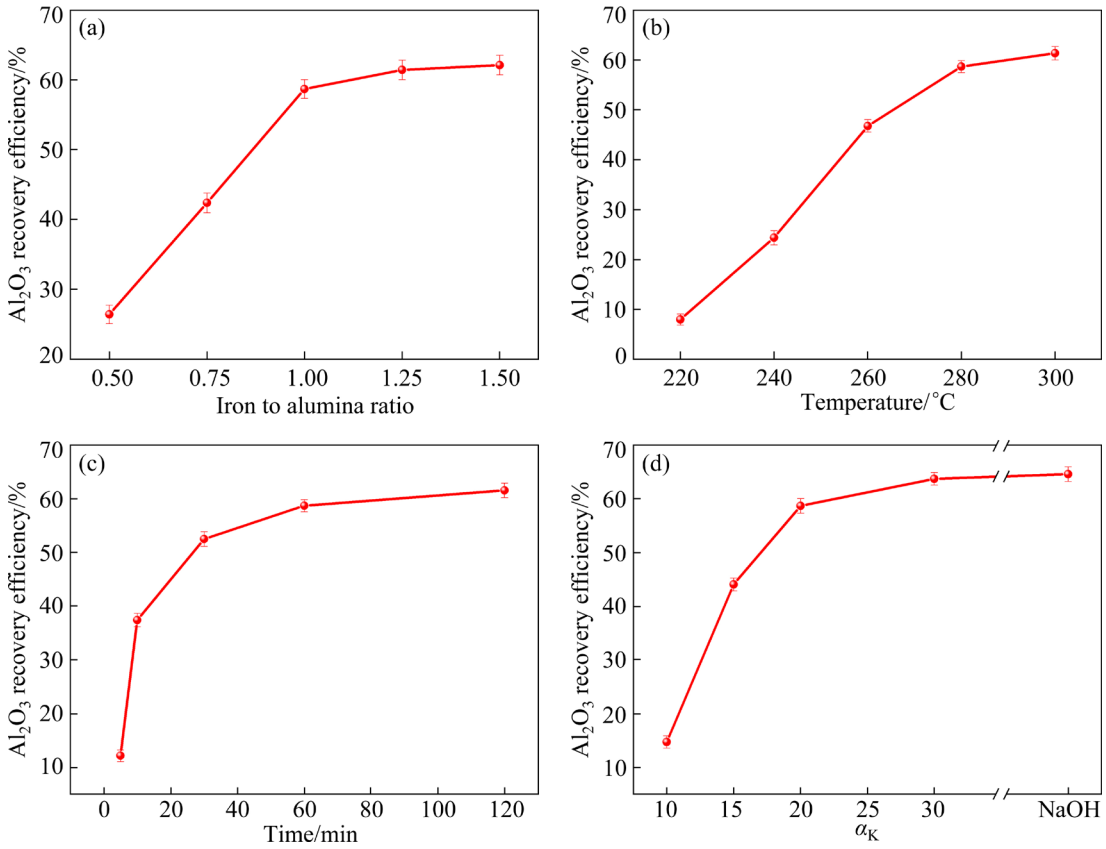

Fig. 6 Al_2O_3 recovery efficiency during conversion from HG to HA: (a) Iron to alumina ratio (T=280 °C, t=60 min and α_K=20); (b) Reaction temperature (F/A=1, t=60 min and α_K=20); (c) Reaction time (F/A=1, T=280 °C, and α_K=20); (d) α_K (F/A=1, T=280 °C and t=60 min)

under different reaction conditions. As presented in Fig. 6(a), the Al_2O_3 recovery efficiency continuously increases as the F/A ratio increases, but it changes little when the F/A ratio surpasses 1.0. The reason is that the substitution reaction of $Fe(OH)_4^-$ to $Al(OH)_4^-$ reaches equilibrium when the F/A ratio is 1.0. As viewed from Fig. 6(b), when the reaction temperature rises from 220 to 280 °C, the Al_2O_3 recovery efficiency increases from 8% to 58.68%. The reaction rate can be expedited by raising the temperature, particularly at the initial reaction stage. As seen from Fig. 6(c), the $Fe(OH)_4^-/Al(OH)_4^-$ substitution reaction takes place quickly at the beginning, and the Al_2O_3 recovery efficiency increases quickly with the prolonged reaction time, especially after 10 min. When the reaction time is prolonged to 60 min, the Al_2O_3 recovery efficiency reaches a maximum level. As shown in Fig. 6(d), as α_K rises, the Al_2O_3 recovery efficiency increases first and then maintains stable. The increasing α_K leads to the decrease of viscosity and diffusion layer thickness in sodium aluminate solution [23]. To realize the phase conversion from HG to HA and synchronous alumina recovery in HG, the optimal conditions are obtained as follows: F/A=1, T=280 °C, t=60 min, α_K=20, and the corresponding Al_2O_3 recovery efficiency reaches 58.68%.

3.3 Conversion mechanism from HG to HA

To reveal the conversion mechanism of HG to HA in the presence of Fe_2O_3, the surface area and surface energy of HG and Fe_2O_3 crystals were calculated, as presented in Figs. 7(a, b). The surface energy of HG and Fe_2O_3 increases first and then maintains stable. As the surface energy of the crystal increases, its adsorption energy also increases. To achieve a stable state, the crystal adsorbs ions present in the solution, thereby reducing its surface energy [26,27]. The binding energy between HG and Fe_2O_3 on the (110) plane is measured to be 81.93 kJ/mol, which is comparatively lower than that on the (104) (198.63 kJ/mol) and (116) (83.97 kJ/mol) planes, indicating that the (110) plane is the significantly exposed face in Fe_2O_3 crystal. During the substitution

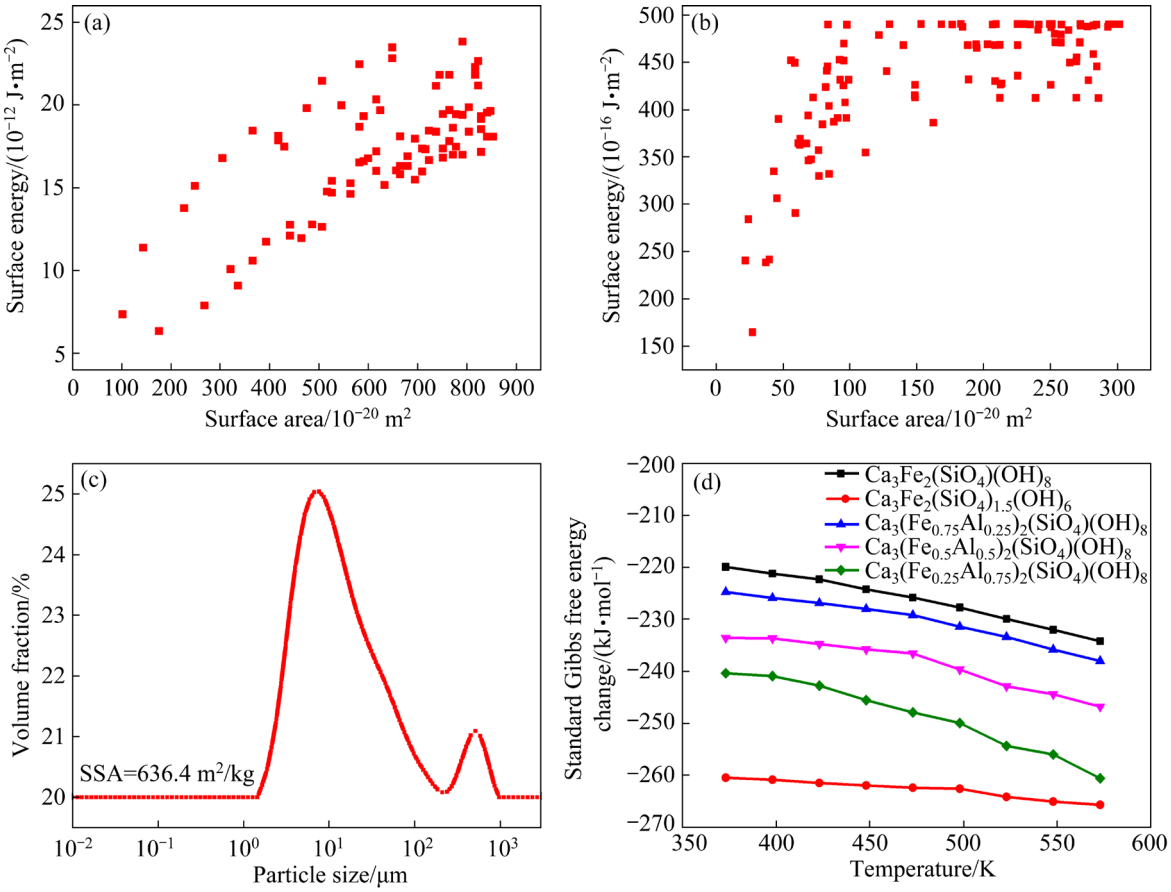

Fig. 7 Surface energy of HG (a) and Fe_2O_3 (b); Particle size distribution of HA (c); Standard Gibbs free energy changes from HG to HA (e)

process, the (110) plane of Fe_2O_3 reacts with HG to cut off the Al—O bond and then releases the $Al(OH)_4^-$ ion. The PSD curve of HA converted from HG under the optimal conditions is illustrated in Fig. 7(c). Compared with the PSD curve of HG (Fig. 4(b)), the particle size of the formed HA decreases and the SSA increases, respectively. According to theory by WEN et al [28], the Gibbs free energy changes of the conversion from HG to HA were calculated in the temperature range from 373 to 573 K, as illustrated in Fig. 7(d). All the Gibbs free energy changes at various temperatures are lower than −210 kJ/mol, indicating that the corresponding reactions are feasible. Meanwhile, they decrease as the reaction temperature increases, indicating that raising the reaction temperature is beneficial for promoting the conversion from HG to HA. Conversely, the increase of iron substitution coefficient in HA results in an increase in the Gibbs free energy changes, suggesting that the HA with a high iron substitution coefficient is more difficult to convert from HG.

Figure 8 illustrates the SEM images of the reaction products acquired during the conversion from HG to HA for different durations, and the corresponding EDS results are listed in Table 3. The reaction products are mainly composed of agglomerated sheet-like particles ranging from a few hundred nanometers to several microns when the reaction time is 5 min (Fig. 8(a)). According to the XRD and EDS results, the block-shaped particles (Point A) are hematite, the surface of which exhibits a high level of smoothness (Fig. 8(b)). Due to the limited time available for crystallization, some HA crystals grow incompletely. The HA particles in Figs. 8(c, d) are formed by the substitution reaction, and their iron contents are low (Points B and C). The HA crystals grow completely when the reaction time is 60 min. As observed in Fig. 8(e), the debris particles with the corresponding molar ratio of Fe_2O_3 to Al_2O_3 close to 2 (Point D) are converted from HG. The Ca/Si ratio of Point D is lower than that of Points B and C, as the prolonged reaction time leads to the increasing silicon saturation coefficient in HA [13].

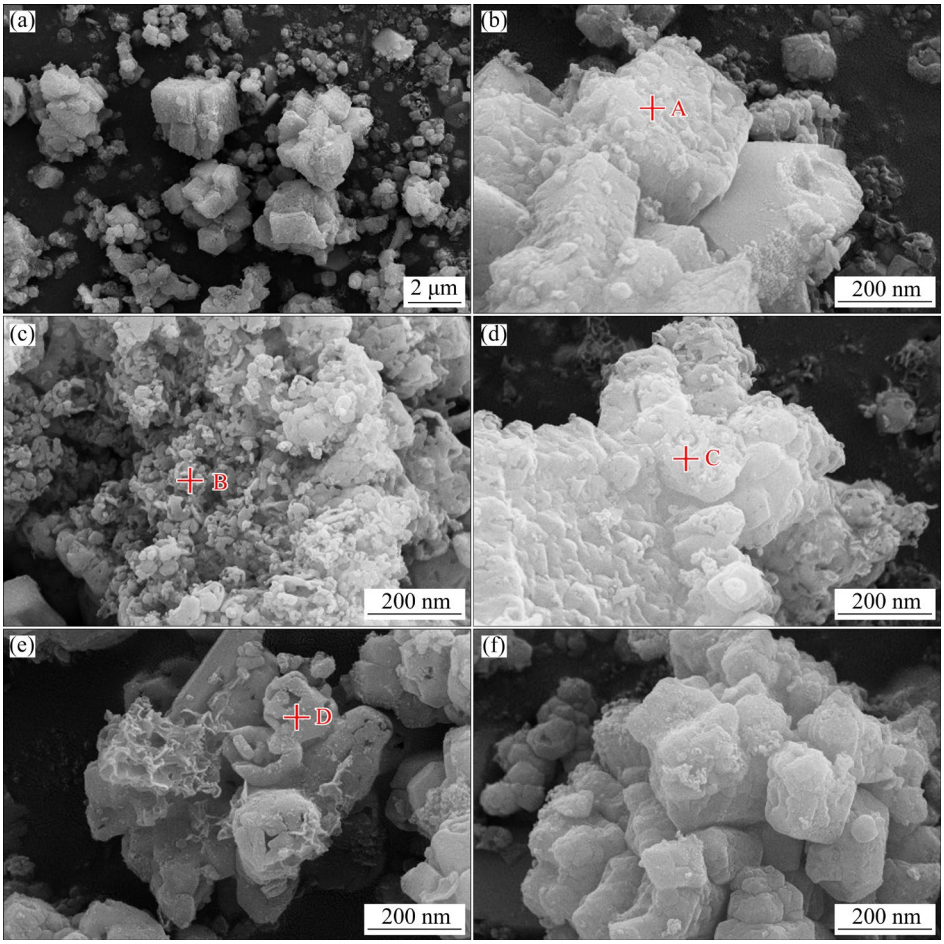

Fig. 8 SEM images of reaction products converted at 280 °C for different reaction time: (a, b, c, d) 5 min; (e, f) 60 min

Table 3 EDS results of different points corresponding to Fig. 8 (at.%)

Point	O	Ca	Al	Si	Fe	Substitution degree
A	59.69	2.95	3.46	1.46	32.75	–
B	70.65	14.00	10.22	4.11	1.02	9.07
C	72.33	12.58	9.59	4.78	0.72	6.98
D	69.39	11.85	4.09	7.67	7.00	63.12

Substitution degree is defined as x(Fe)/x(Al+Fe)×100%

As presented in Fig. 8(f), a large number of well crystallized spherical aggregates appear, indicating that the substitution reaction of $Fe(OH)_4^-$ to $Al(OH)_4^-$ gradually reaches the equilibrium when the reaction time is 60 min. Thus, the conversion from HG to HA is positively impacted by the reaction time.

According to the above results, the conversion process from HG to HA corresponds closely to the HA formation in sodium aluminate solution [13,15]. The conversion mechanism is illustrated in Fig. 9. The formation of HA occurs by the substitution of $Fe(OH)_4^-$ for $Al(OH)_4^-$ in HG. The HG maintains unsteady layered structure for the Ca—O band and Al—O bond, and the released $Al(OH)_4^-$ ion selectively migrates to $Fe(OH)_4^-$ ion in sodium aluminate solution. Simultaneously, generous $Fe(OH)_4^-$ ion present in the solution can effectively penetrate the Al—O octahedron, leading to the formation of HA. The length of Fe—O bond (0.1971 nm) formed in HA is smaller than that of Al—O bond (0.1987 nm), which is beneficial to increase the structural stability of HA crystal.

3.4 Novel process to recover alumina from RM

In order to recover alumina from RM based on the conversion from HG to HA, the RM was treated under the optimal reaction conditions. The sodium ferrite was not added because of the abundant iron oxide in RM. The chemical compositions and XRD patterns of RM before and after treatment are presented in Table 4 and Fig. 10. As listed in Table 4, the Al_2O_3 content in initial RM is 17.82%, with an initial A/S ratio of 1.64 and N/S ratio (the mass ratio

of Na_2O to SiO_2) of 0.45. The contents of Al_2O_3 and Na_2O in the treated RM are reduced to 6.57% and 0.13%, respectively. The corresponding Al_2O_3 and Na_2O recovery efficiencies are 63.06% and 97.34%, and the A/S ratio in the treated RM is only 0.60. As shown in Fig. 10(a), the phases present in RM mainly include sodium aluminosilicate hydrate ($1.08Na_2O{\cdot}Al_2O_3{\cdot}1.68SiO_2{\cdot}1.8H_2O$), HG ($3CaO{\cdot}Al_2O_3{\cdot}SiO_2{\cdot}4H_2O$), hematite ($Fe_2O_3$) and perovskite ($CaTiO_3$). As illustrated in Fig. 10(b), most of HG is converted into HA ($Ca_3(Fe_{0.87}Al_{0.13})_2(SiO_4)_{1.65}(OH)_{5.4}$) after the hydrothermal treatment, while the sodium aluminosilicate hydrate is dissolved. In comparison, the Al_2O_3 recovery efficiency from RM

Table 4 Chemical compositions of RM before and after treatment (wt.%)

Red mud	Al_2O_3	SiO_2	Fe_2O_3	TiO_2	CaO	Na_2O	LOI
Before treatment	17.82	10.88	37.23	5.36	11.79	4.88	9.96
After treatment	6.57	10.86	36.77	5.15	27.83	0.13	11.01

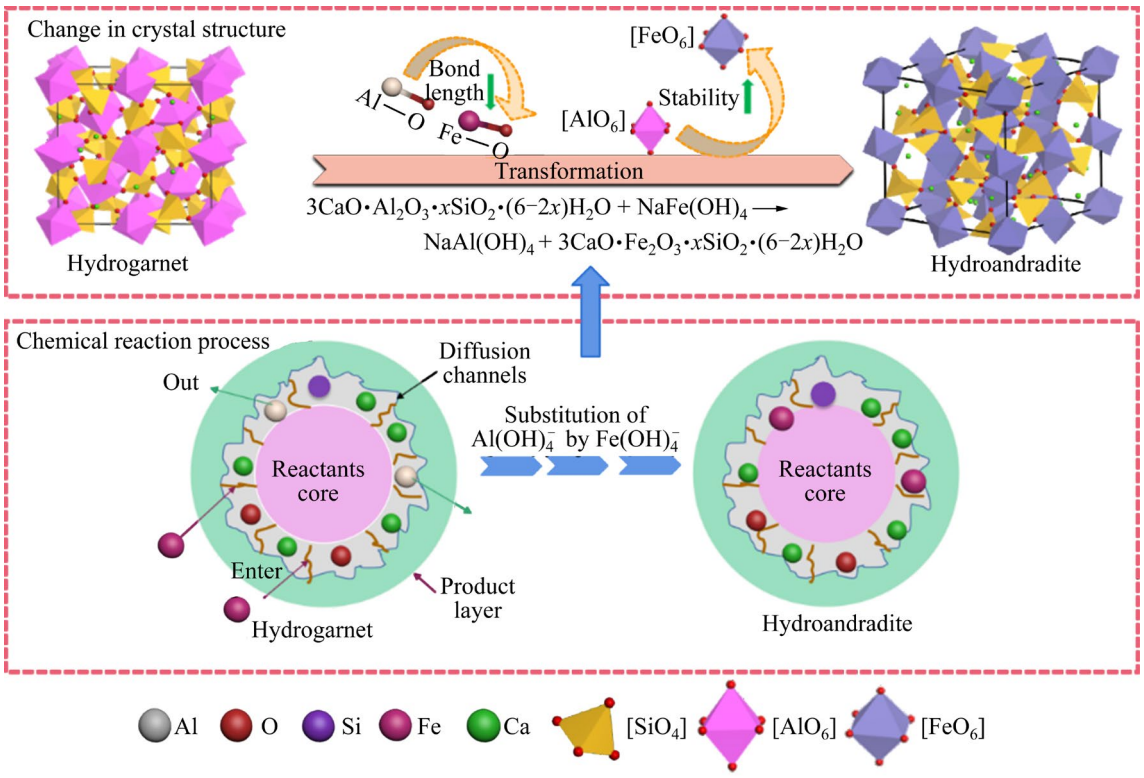

Fig. 9 Schematic diagram of conversion mechanism from HG to HA

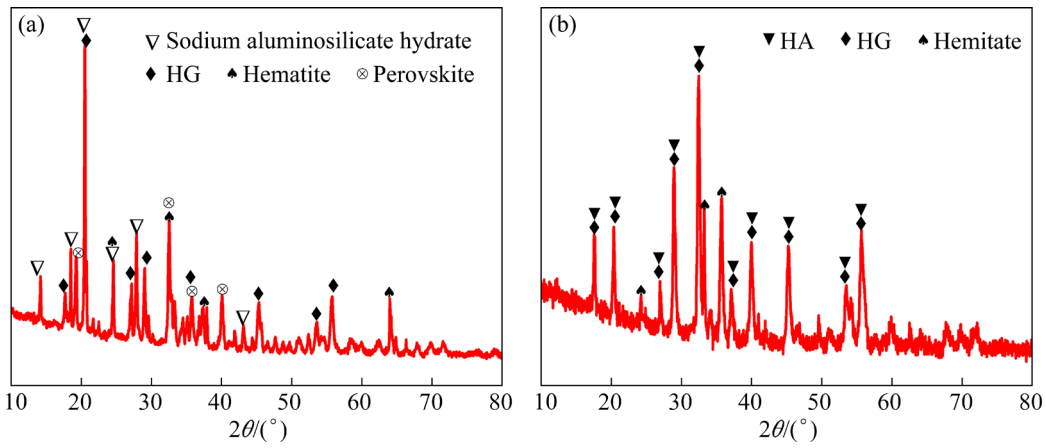

Fig. 10 XRD patterns of RM before (a) and after (b) treatment

is higher than that from HG, because the Al_2O_3 in sodium aluminosilicate hydrate can also be recovered during the hydrothermal process. Meanwhile, the sodium aluminosilicate hydrate dissolved in sodium aluminate solution can directly form HA with lower solubility by spontaneous nucleation [13].

As presented in Fig. 11, the initial RM is present in various shapes and sizes including block and flocculent particles (Fig. 11(a)). The elemental mappings reveal that the contents of Si and Al are comparatively higher than those of other elements (Figs. 11(b−f)). As shown in Figs. 11(g, h), the distribution and particle size of RM after treatment are relatively uniform, and the HA with a sheet-like morphology is remarkably different from that of the initial RM.

A comparison between the new hydrothermal process and other existing processes is listed in Table 5. It has the characteristics of short process,

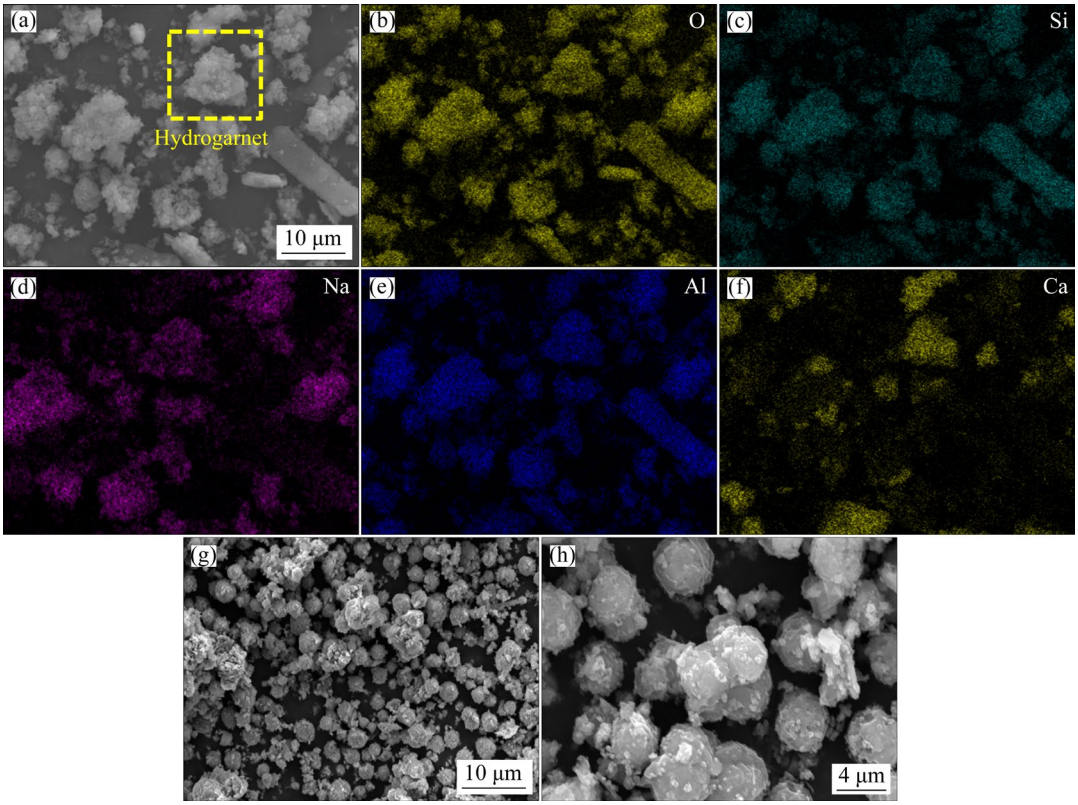

Fig. 11 SEM−EDS images of RM before (a−f) and after (g, h) treatment

Table 5 Comparison between hydrothermal process and other typical processes

Process	Advantage	Disadvantage	Technological condition	Recovery efficiency	Economy evaluation
Lime-soda process	Mature technology	High energy consumption; Large amount of slag	1200 °C; C/S=2	Al_2O_3 >80%; Na_2O >90%	Poor
Sub-molten salt process	Hydrometallurgical process	Complex production process; High-level equipment	210−230 °C; Initial NaOH concentration: 50%−70%	Al_2O_3 >60%; Na_2O >90%	Normal
Acid process	Low energy consumption; Easy operation	Difficult to separate metals; Equipment corrosion	<100 °C	Al_2O_3 >50%; Na_2O >90%	—
Hydrothermal process	Hydrometallurgical process; Short production process	—	220−260 °C	Al_2O_3 >60%; Na_2O >90%	Good

low energy consumption and production cost. Approximately 50 kg Na_2O and 120 kg Al_2O_3 can be recovered from 1 t RM by the hydrothermal process. Additionally, the CO_2 emissions and energy consumption in the new process are significantly lower than those by the sintering process. Compared with the Na_2O recovery methods of activating roasting−water leaching and electrodialysis from RM, the Na_2O recovery efficiency in this work is much larger than that by ZHU et al [29] (82.00%) and ZHANG et al [30] (76.62%).

4 Conclusions

(1) The HA with varied silicon saturation coefficients is more stable than HG, and the Si—O bond has a significant impact on the structural stability of HG and HA. The (110) plane of Fe_2O_3 is easier to combine with HG to form HA. The phase conversion from HG to HA is improved by the reaction temperature, and the HA with a high iron substitution coefficient is more difficult to be converted from HG.

(2) The optimal conditions of the phase conversion from HG to HA in the synthetic sodium aluminate solution are as follows: F/A=1, T=280 °C, t=60 min, and α_K=20, and the corresponding Al_2O_3 recovery efficiency reaches 58.68%.

(3) A novel hydrothermal process is proposed for the synergistic recovery of Al_2O_3 and Na_2O from diasporic-bauxite-type RM based on the phase conversion from HG to HA. The recovery efficiencies of Al_2O_3 and Na_2O are 63.06% and 97.34%, respectively.

CRediT authorship contribution statement

Hong-fei WU: Investigation, Data curation, Writing − Original draft; **Xiao-lin PAN:** Conceptualization, Supervision, Funding acquisition, Writing − Review & editing; **Ji-long LIU:** Investigation, Data curation; **Feng QIU:** Investigation, Data curation; **Tun HE:** Investigation, Data curation; **Hai-yan YU:** Conceptualization, Funding acquisition.

Declaration of competing interest

The authors declare that they have no known competing financial interests or personal relationships that could have appeared to influence the work reported in this paper.

Acknowledgments

The authors greatly appreciate the financial support from the National Key R&D Program of China (No. 2022YFC2904405), and the National Natural Science Foundation of China (Nos. 22078055, 51774079).

References

[1] DENG B N, LI G H, LUO J, QING Y, LIU M X, RAO M J, JIANG T, BAUMAN L, ZHAO B X. Selectively leaching the iron-removed bauxite residues with phosphoric acid for enrichment of rare earth elements [J]. Separation and Purification Technology, 2019, 227: 115714−115720.

[2] PAN Xiao-lin, WU Hong-fei, LV Zhong-yang, YU Hai-yan, TU Gan-feng. Recovery of valuable metals from red mud: A comprehensive review [J]. Science of the Total Environment, 2023, 904: 166686.

[3] RAI S, NIMJE M T, CHADDHA M J, MODAK S, RAO K R, AGNIHOTRI A. Recovery of iron from bauxite residue using advanced separation techniques [J]. Minerals Engineering, 2019, 134: 222−231.

[4] HABIBI H, MOKMELI M, SHAKIBANIA S, PIROUZAN D, POURKAIMI Z. Separation and recovery of titanium and scandium from the red mud [J]. Separation and Purification Technology, 2023, 317: 123882.

[5] JIANG Tao, PAN Xiao-lin, WU Yan, YU Hai-yan, TU Gan-feng. Mineral conversion of desilication products precipitated in synthetic sodium aluminate solution under atmospheric pressure [J]. Transactions of Nonferrous Metals Society of China, 2018, 28(2): 367−375.

[6] PAN Xiao-lin, WU Hong-fei, YU Hai-yan, BI Shi-wen. Precipitation of desilication products in $CaO−Na_2O−Al_2O_3−SiO_2−H_2O$ system based on the Bayer process [J]. Hydrometallurgy, 2020, 197: 105469.

[7] KLIMESCH D S, RAY A. DTA–TGA of unstirred autoclaved metakaolin–lime–quartz slurries. The formation of hydrogarnet [J]. Thermochim Acta, 1998, 316(2): 149−154.

[8] LI Xiao-bin, YU Shun-wen, DONG Wen-bo, CHEN Yong-kun, ZHOU Qiu-sheng, QI Tian-gui, LIU Gui-hua, PENG Zhi-hong, JIANG Yong-yong. Investigating the effect of ferrous ion on the digestion of diasporic bauxite in the Bayer process [J]. Hydrometallurgy, 2015, 152: 183−189.

[9] SMITH P. Reactions of lime under high temperature Bayer digestion conditions [J]. Hydrometallurgy, 2017, 170: 16−23.

[10] WHITTINGTON B, FALLOWS T. Formation of lime-containing desilication product (DSP) in the Bayer process: Factors influencing the laboratory modelling of DSP formation [J]. Hydrometallurgy, 1997, 45: 289−303.

[11] WANG Yi-chuan. Raman scattering of grossular-andradite solid solution [J]. Chinese Journal of High Pressure Physics, 2020, 34(4): 3−11. (in Chinese)

[12] LI Xin-hua, GU Song-qing, YIN Zhong-lin, WU Guo-bao, ZHAI Yu-chun. Regulating the digestion of high silica bauxite with calcium ferrite addition [J]. Hydrometallurgy, 2010, 104: 313−316.

[13] PAN Xiao-lin, WU Hong-fei, LIU Ji-long, LIU Qing-wen, YU Hai-yan. Hydrothermal formation mechanism of the efficient desilication product hydroandradite

($3CaO·Fe_2O_3·xSiO_2·(6−2x)H_2O$) [J]. Hydrometallurgy, 2021, 203: 105695.
[14] XU B A, SMITH P. The effect of iron sources on caustic and alumina recovery from synthetic Bayer DSP (sodalite) [J]. Hydrometallurgy, 2012, 129: 26−29.
[15] WU Hong-fei, PAN Xiao-lin, ZHU Mi-mi, YU Hai-yan. Structural stability and electronic properties of complex silicate compound of hydroandradite [J]. Materials Today Communications, 2023, 36: 106878.
[16] DILNESA B Z, LOTHENBACH B, RENAUDIN G, WICHSER A, KULIK D. Synthesis and characterization of hydrogarnet $Ca_3(Al_xFe_{1-x})_2(SiO_4)_y(OH)_{4(3-y)}$ [J]. Cement and Concrete Research, 2014, 59: 96−111.
[17] ZHANG Ren, ZHENG Shi-li, MA Shu-hua, ZHANG Yi. Recovery of alumina and alkali in Bayer red mud by the formation of andradite-grossular hydrogarnet in hydrothermal process [J]. Journal of Hazardous Materials, 2011, 189: 827−835.
[18] DAI X, NHUNG N T H, HAMZA M F, GUO Y X, CHEN L, HE C L, NING S Y, WEI Y Z, DODBIBA G, FUJITA T. Selective adsorption and recovery of scandium from red mud leachate by using phosphoric acid pre-treated pitaya peel biochar [J]. Separation and Purification Technology, 2022, 292: 121043.
[19] PAN Yong, WANG Shuang-lun, ZHANG Xi, JIA Lin-hu. First-principles investigation of new structure, mechanical and electronic properties of Mo-based silicides [J]. Ceramics International, 2017, 44: 1744−1750.
[20] QI Chong-chong, XU Xin-hang, CHEN Qiu-song. Hydration reactivity difference between dicalcium silicate and tricalcium silicate revealed from structural and Bader charge analysis [J]. International Journal of Minerals Metallurgy and Materials, 2022, 29(2): 335−344.
[21] PENG H, VAUGHAN J. Aluminate effect on desilication product phase conversion [J]. Journal of Crystal Growth, 2018, 492: 84−91.
[22] SAMILI R, VAUGHAN J. Crystallisation of tricalcium aluminate from sodium aluminate solution using slaked lime [J]. Powder Technology, 2016, 294: 472−483.
[23] LI Xiao-bin, WANG Dan-qin, ZHOU Qiu-sheng, LIU Gui-hua, PENG Zhi-hong. Concentration variation of aluminate ions during the seeded precipitation process of gibbsite from sodium aluminate solution [J]. Hydrometallurgy, 2011, 106: 93−98.
[24] XU Ying-peng, CHEN Chao-yi, LAN Yuan-pei, WANG Lin-zhu, LI Jun-qi. Desilication and recycling of alkali-silicate solution seeded with red mud for low-grade bauxite utilization [J]. Journal of Materials Research and Technology, 2020, 9: 7418−7426.
[25] ZHENG K L, GERSON A R, ADDAI-MENSAH J, SMART R S C. The influence of sodium carbonate on sodium aluminosilicate crystallisation and solubility in sodium aluminate solutions [J]. Journal of Crystal Growth, 1997, 171: 197−208.
[26] DAI Jia, LI Ke, HAN Wen-duo, LI Yao-hui, LI Yi-fan, HU Zhi. First-principles investigation on the structural, electronic, mechanical and thermodynamic properties of binary phase in Mg−1Si−3RE (RE=La, Ce) alloys [J]. Materials Today Communications, 2021, 26: 101738.
[27] WU Hong-fei, CHEN Chao-yi, LI Jun-qi, LAN Yuan-pei, WANG Lin-zhu, QUAN Bian-li, JIN Hui-xin. Digestion mechanism and crystal simulation of roasted low-grade high-sulfur bauxite [J]. Transactions of Nonferrous Metals Society of China, 2020, 30(6): 1662−1673.
[28] WEN Yuan-kai, SHAO Jun, WANG San-shan, CHEN De-wei. A simplified formula to calculate heat formation of oxyacid salt and mineral [J]. Acta Metallurgica Sinica, 1979, 15: 98−108. (in Chinese)
[29] ZHU Xiao-bo, LI Wang, GUAN Xue-mao. An active dealkalization of red mud with roasting and water leaching [J]. Journal of Hazardous Materials, 2015, 286: 85−91.
[30] ZHANG Y X, SHI Q, LUO M X, WANG H T, QI X J, HOU C H, LI F T, AI Z S, JUNIOR J T A. Improved bauxite residue dealkalization by combination of aerated washing and electrodialysis [J]. Journal of Hazardous Materials, 2019, 364: 682−690.

基于赤泥回收氧化铝的水化石榴石向钙铁榴石水热转化

吴鸿飞[1,2,3]，潘晓林[1,2,3]，刘吉龙[1,2,3]，邱 峰[1,2,3]，何 屯[2]，于海燕[1,2,3]

1. 东北大学 多金属共生矿生态化冶金教育部重点实验室，沈阳 110819；
2. 东北大学 冶金学院，沈阳 110819；
3. 沈阳市有色金属资源循环利用重点实验室，沈阳 110819

摘 要：为了同步回收赤泥中的氧化铝和碱，利用第一性原理、XRF、XRD、PSD 和 SEM 等手段研究了水化石榴石(HG)和钙铁榴石(HA)的结构稳定性与转化机制，并基于转化原理提出了一种新型水热转化工艺。晶体结构模拟表明，不同硅饱和系数的 HA 比 HG 更稳定且 HG 不能转化为高铁取代度的 HA。水热转化过程 Fe_2O_3 (110)晶面更易与 HG 结合形成 HA，结合能为 81.93 kJ/mol。揭示了原料配比、溶液成分和水热转化参数对 HG 向 HA 水热转化的影响，并获得了氧化铝回收的最佳条件。赤泥中氧化铝和氧化钠回收率分别为 63.06%和 97.34%，处理后赤泥中的 Na_2O 含量仅为 0.13%。

关键词：水化石榴石；钙铁榴石；结构稳定性；水热转化；赤泥

(Edited by Bing YANG)